PHYSICAL REVIEW B VOLUME 23, NUMBER 8 15 APRIL 1981

Lattice dynamics of graphite slabs

E. de Rouffignac
Instituto Mexicano del Petróleo, Investigacion Basica de Procesor, AP 14-805, México, Distrito Federal, México

G. P. Alldredge
Department of Physics, University of Missouri at Columbia, Columbia, Missouri 65211

F. W. de Wette
Department of Physics, University of Texas, Austin, Texas 78712

(Received 13 June 1980)

Finely divided graphite is one of the most useful materials for a wide variety of adsorption studies. As a major step in our investigations of the theoretical description of such adsorption phenomena, we present here full dynamical calculations of bulk graphite and of graphite slabs consisting of a finite number of (0001) graphite planes. An extended version of the axially symmetric model of Nicklow, Wakabayashi, and Smith allows the appearance of surface modes of vibration not found with simpler models. Six branches of surface modes are found, but the surface modes are much less pronounced than those in more isotropic crystals as a result of the very weak interaction between the planes. We also present the bulk and slab vibrational density-of-states functions.

I. INTRODUCTION

For many years finely divided graphites—graphitized carbon blacks and, more recently, exfoliated graphites—have been widely used as substrate materials for adsorption studies, because the exposed surfaces in these materials are predominantly the well characterized (0001) basal plane surfaces. These have the advantage that surface uniformity can be controlled by heat treatment or annealing, and that, because of this uniformity, the modeling of adsorbate-adsorbent interactions is greatly facilitated. These circumstances have led, over the years, to the accumulation of a large body of data in the form of adsorption isotherms and heats of adsorption for a variety of gases adsorbed on graphite substrates. Although such work has been very useful for the study of adsorbate-adsorbent interactions, a new approach has recently received increasing attention, namely, the direct measurement of the thermal properties of the adsorbed material, such as heat-capacity measurements. Experimental results of this kind are based on measurements of the thermal properties of a system exhibiting large surface-area-to-volume ratio; the contribution due to the adsorbed species is then obtained by subtracting from the measured quantity of the total adsorbate-adsorbent system the contribution due to the bare adsorbent. The same procedure is followed in the theoretical evaluation of surface- and adsorbate-thermodynamic properties.

In the case of graphitic substrates, it has usually been assumed that the substrate is inert in that the dynamics of the substrate does not contribute significantly to measurements of properties of adsorbed systems. Such an assumption must be valid to a reasonable first approximation, because data analyses based on it have been reasonably consistent with experience. However, with increasing refinement and sensitivity of experimental methods, there is an increasing need for quantitative evaluation of the validity of such inert-adsorbent approximations. This is important both to establish bounds on the validity of such assumptions in interpreting experiments and to prepare the way for data analyses which can take account of substrate dynamics.

The present paper deals with the first aspect of such a theoretical evaluation, namely, the lattice-dynamical treatment of a graphite system with a high surface-to-volume ratio. Aside from the interest of such systems for adsorption studies, they are of intrinsic interest because of the changes in their thermodynamic properties caused by the large surface areas of the "bare" materials. For instance, measurements of the heat capacities of graphite samples of various states of subdivision have been made by De Sorbo and Nichols,[1] van der Hoeven and Keesom,[2] Delhaes and Hishiyama,[3] and Wostenholm and Yates.[4] Discrepancies found in the heat capacities reported by these various authors have been attributed to differences in sample treatment. Various explanations have been suggested to account for these differences: For instance, it has been suggested that some of these discrepancies may be the effect of adsorbed impurities. A different explanation was proposed by Komatsu,[5] who showed that an increase in the specific heat can result from a reduction in the values of the interplanar elastic constants c_{33} and c_{44}, caused by the presence of stacking faults. On the other hand, Flubacher *et al.*[6] have suggested that in clean samples the excess specific heats could well be due to intrinsic surface effects rather than to changes in the elastic constants.

As a step in investigating this question and others concerning a bare graphite substrate, we present here a full lattice-dynamical treatment of a graphite system with surfaces. More precisely, we deal with a graphite slab of a finite but significant number of atomic layers, bounded by two free (0001) basal plane surfaces and infinitely extended in the directions parallel to the basal planes. Such a full treatment goes beyond earlier works, such as Refs. 7 and 8, which focus on more limited questions or more simplified models. The lattice treatment of such a slab with a registered phase of xenon atoms absorbed on its surfaces, as well as a discussion of the thermodynamic properties of the bare slab and the xenon-covered slab, will be presented in subsequent publications. Some of the more significant preliminary results of these studies have been given in a recent publication.[9]

In Secs. II and III we present, respectively, discussions of the lattice dynamics of bulk graphite, and of the graphite slab. A general discussion and conclusions follow in Sec. IV.

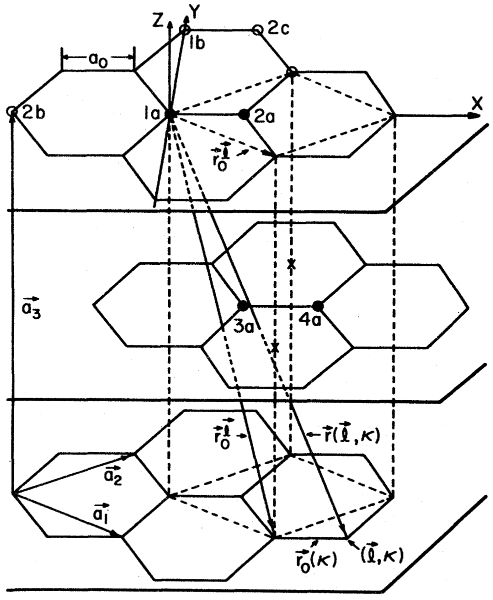

FIG. 1. Bulk graphite unit cell.

II. BULK GRAPHITE

The hexagonal structure of graphite consists of stacked planes consisting of covalently bonded carbon atoms, the planes being held together by dispersion (van der Waals) forces. A variety of force-constant models has been used to describe these intraplanar (in-plane) and interplanar (out-of-plane) carbon-carbon interactions. Although a "valence force field" model is appropriate to describe the intraplanar interactions, in the present work we have chosen to use the "axially symmetric" (AS) pairwise interaction model of Nicklow, Wakabayashi, and Smith[10] (NWS), because it is based on a fit to their incomplete, but nevertheless extensive, measurements of phonon dispersion curves, which constitute the most complete set of measurements to date. Furthermore, as pointed out by these authors, the (bulk) specific heat of graphite deduced from their model reproduces almost exactly the experimental behavior over a wide range of temperatures (1.5–300 K).

A. The graphite lattice

The geometry of the bulk graphite primitive unit cell is shown in Fig. 1 together with the primitive lattice vectors $\vec{a}_1, \vec{a}_2, \vec{a}_3$. The nearest-neighbor distance is given by a_0 and the interplanar distance by c, where, according to Ref. 11,

$$a_0 = 1.4210 \pm 0.0001\ \text{Å}\,, \qquad c = 3.3539 \pm 0.0007\ \text{Å}\,. \tag{1}$$

The primitive lattice vectors, in terms of the indicated Cartesian system, are given by

$$\vec{a}_1 = \left(\frac{3}{2}a_0, -\frac{\sqrt{3}}{2}a_0, 0\right)\,,$$

$$\vec{a}_2 = \left(\frac{3}{2}a_0, \frac{\sqrt{3}}{2}a_0, 0\right),$$

$$\vec{a}_3 = (0, 0, 2c)\,. \tag{2}$$

There are four atoms (labeled 1 through 4) in the unit cell, located at

$$\text{atom } 1a\ (0,0,0)\,, \quad \text{atom } 2a\ (a_0,0,0)\,, \quad \text{atom } 3a\ (a_0,0,-c)\,, \quad \text{atom } 4a\ (2a_0,0,-c)\,. \tag{3}$$

The AS interaction model of NWS considers intraplanar interactions up to third neighbors, but only first-neighbor interplanar interactions. We have extended the model to include second-neighbor interplanar interactions for the following reasons: First, the second-interplanar-neighbor distance is less than 10% larger than the first-interplanar-neighbor distance. Second, not only does an atom that has only two first-interplanar neighbors have six second-interplanar neighbors, but in addition an atom that has no interplanar neighbor at a distance of c has twelve interplanar neighbors at the second-interplanar-neighbor distance. Hence these interactions should not be neglected. Finally, of specific interest to the dynamics, the first-interplanar neighbors do not couple atomic motions parallel to the crystal layer to those perpendicular to it, whereas second-interplanar interactions do give rise to this coupling, and consequently to surface modes of vibration, not resulting from the original model. A survey of the carbon-carbon interactions used in our model is given in Table I.

B. Bulk lattice dynamics

We consider a crystal built up of unit cells, labeled by the triad of integers $\vec{l}=(l_1, l_3, l_3)$, each containing s different atoms labeled by κ. The instantaneous position of the atom κ in the unit cell $\vec{l}$ [atom $(\vec{l}\kappa)$] is given by

$$\vec{r}(\vec{l}\kappa)=\vec{r}_0(\vec{l}\kappa)+\vec{u}(\vec{l}\kappa),$$

where $\vec{r}_0(\vec{l}\kappa)$ is the mean position of atom $(\vec{l}\kappa)$ and $\vec{u}(\vec{l}\kappa)$ its instantaneous displacement from the mean position. In the quasiharmonic approximation the total potential energy of the crystal is expanded in a Taylor series in $u_\alpha(\vec{l}\kappa)$ $(\alpha, \beta=x, y, z)$ up to the quadratic term

$$\Phi=\Phi_0+\sum_{\vec{l}\kappa\alpha}\Phi_\alpha(\vec{l}\kappa)u_\alpha(\vec{l}\kappa) +\tfrac{1}{2}\sum_{\vec{l}\kappa\alpha}\sum_{\vec{l}'\kappa'\beta}\Phi_{\alpha\beta}(\vec{l}\kappa, \vec{l}'\kappa')u_\alpha(\vec{l}\kappa)u_\beta(\vec{l}'\kappa'), \tag{4}$$

where

$$\Phi_\alpha(\vec{l}\kappa)=\frac{\partial\Phi}{\partial u_\alpha(\vec{l}\kappa)}\bigg|_0, \tag{5}$$

$$\Phi_{\alpha\beta}(\vec{l}\kappa;\vec{l}'\kappa')=\frac{\partial^2\Phi}{\partial u_\alpha(\vec{l}\kappa)\partial u_\beta(\vec{l}'\kappa')}\bigg|_0. \tag{6}$$

The subscript on the derivatives indicates that they are taken for the atoms in their mean positions. The $\Phi_\alpha(\vec{l}\kappa)$ are zero if the crystal is in static equilibrium ($T=0$ K, zero-point dilation neglected) and at finite temperatures, if in addition $(\vec{l}\kappa)$ is a center of inversion; in general the Φ_α are small and they will be neglected. The $\Phi_{\alpha\beta}$ are the force constants that appear in the equations of motion.

The vibrational frequencies $\omega_p(\vec{q})$ of the crystal are obtained from the eigenvalue equation

$$\sum_{\kappa'\beta}D_{\alpha\beta}(\kappa\kappa';\vec{q})\xi_\beta(\kappa';\vec{q}p)=\omega_p^2(\vec{q})\xi_\alpha(\kappa;\vec{q}p). \tag{7}$$

Here $\xi_\alpha(\kappa;\vec{q}p)$ is the α component of the polarization vector of atom κ in the mode characterized by the wave vector $\vec{q}$ and the polarization index p $(=1, 2, \ldots, 3s)$. $D_{\alpha\beta}$ is the dynamical matrix element defined by

$$D_{\alpha\beta}(\kappa\kappa';\vec{q})=(M_\kappa M_{\kappa'})^{-1/2}\sum_{\vec{l}'}\Phi_{\alpha\beta}(\vec{l}\kappa;\vec{l}'\kappa')\exp\{i\vec{q}\cdot[\vec{r}_0(\vec{l}'\kappa')-\vec{r}_0(\vec{l}\kappa)]\}, \tag{8}$$

where M_κ and $M_{\kappa'}$ are the masses of atoms κ and κ', respectively. The order of the dynamical matrix is equal to the maximum value of p, i.e., $3s$; for bulk graphite with four atoms per unit cell the order is 12.

The AS interaction model assumes that the force constants are derived as if the atoms interact through central potentials, i.e., that the forces between two atoms can be derived from a pairwise interaction potential function $\phi(r)$ which depends only on the distance r between the two atoms.

Different potential functions are used for different shells of neighbors. Let the potential of interaction between the atoms κ and κ' be denoted by $\phi_{\kappa\kappa'}(r)$; then the total potential energy of the crystal can be written as

$$\Phi=\sum_{\vec{l}\kappa}\sum_{\vec{l}'\kappa'(\neq\vec{l}\kappa)}\phi_{\kappa\kappa'}(|\vec{r}(\vec{l}\kappa)-\vec{r}(\vec{l}'\kappa')|). \tag{9}$$

Maradudin *et al.*,[12] show that under these conditions we have the following expression for the force constants $\Phi_{\alpha\beta}$:

TABLE I. Carbon-carbon interactions in graphite.

	Interaction type[a]	Neighbor order	Number of neighbors	Interatomic distance
Intraplanar interactions	$1a$-$2a$	1st	3	a_0
	$1a$-$1b$	2nd	6	$3a_0$
	$2a$-$2c$	2nd	6	$3a_0$
	$1a$-$2b$	3rd	3	$2a_0$
Interplanar interactions	$2a$-$3a$	1st	2	c
	$1a$-$3a$ $2a$-$4a$	2nd	12 6	$(a_0^2+c^2)^{1/2}$

[a] For locations of atoms, see Fig. 1.

$$\Phi_{\alpha\beta}(\vec{l}\kappa;\vec{l}'\kappa')=-\left[\frac{r_\alpha r_\beta}{r^2}\left(\phi''_{\kappa\kappa'}(r)-\frac{1}{r}\phi'_{\kappa\kappa'}(r)\right)+\frac{\delta_{\alpha\beta}}{r}\phi'_{\kappa\kappa'}(r)\right]\Bigg|_{r=r_0(\vec{l}\kappa,\vec{l}'\kappa')}, \tag{10}$$

where r is the distance between the atoms $(\vec{l}\kappa)$ and $(\vec{l}'\kappa')$, and r_0 the distance between their mean positions. Equation (10) can be simplified by writing

$$\phi_r^n=[\phi''(r)]_{r=r_n}=\left(\frac{d^2\phi(r)}{dr^2}\right)_{r=r_n}, \tag{11}$$

$$\phi_t^n=\left(\frac{\phi'(r)}{r}\right)_{r=r_n}=\left(\frac{1}{r}\frac{d\phi(r)}{dr}\right)_{r=r_n}, \tag{12}$$

where r_n is the distance between atoms which are nth neighbors of each other. The atomic positions given in Eq. (3) now lead to the following interaction constants:

$$\begin{aligned}
&\alpha_1=-\phi_r^1,\quad \beta_1=-\phi_t^1,\quad \gamma_1=-\phi_t^1,\\
&\alpha_2=-\phi_t^2,\quad \beta_2=-\phi_t^2,\quad \gamma_2=-\phi_t^2,\\
&\alpha_3=-\phi_t^3,\quad \beta_3=-\phi_t^3,\quad \gamma_3=-\phi_t^3,\\
&\alpha_4=-\phi_t^4,\quad \gamma_4=-\phi_r^4,\\
&\alpha_5=-\left(\phi_t^5+\frac{a_0^2}{c^2+a_0^2}(\phi_r^5-\phi_t^5)\right),\\
&\beta_5=-\phi_t^5,\\
&\gamma_5=-\left(\phi_t^5+\frac{c^2}{c^2+a_0^2}(\phi_r^5-\phi_t^5)\right),\\
&\epsilon_5=-\frac{a_0c}{a_0^2+c^2}(\phi_r^5-\phi_t^5).
\end{aligned} \tag{13}$$

The values of ϕ_r^i and ϕ_t^i $(i=1,2,3,4)$ were evaluated by NWS by fitting their model to experimental data comprised of their partial (up to about 14 THz) dispersion curves obtained from inelastic neutron scattering, the Raman frequency (1575 cm^{-1}), and an observed value for the c_{66} elastic constant.

As explained above, it was necessary to modify the NWS model by introducing second-interplanar neighbor interactions. In order to do this the intraplanar force constants were left unmodified. The new values of ϕ_t^4 and ϕ_r^4 were found to give roughly the correct frequencies for the TO and the LO modes at Γ (the origin of wave-vector space), within the new five-neighbor model. Then keeping ϕ_t^4 and ϕ_r^4 fixed, we varied ϕ_t^5 and ϕ_r^5 in order to obtain a best fit to the previously mentioned frequencies at Γ. These frequencies were chosen for the fit because low frequencies are most likely to be affected by strengthening of the interplanar interactions. The result of these modifications are given in Table II.

TABLE II. Force constants for graphite (10^5 dyn/cm).

	This work	NWS[a]
α_1	−3.62	−3.62
β_1	−1.99	−1.99
α_2	0.52	0.52
β_2	−1.33	−1.33
α_3	0.037	0.037
β_3	−0.288	−0.288
α_4	5.99×10^{-4}	-7.7×10^{-3}
γ_4	-1.947×10^{-2}	-5.8×10^{-2}
α_5	-1.076×10^{-3}	
β_5	-7.67×10^{-4}	
γ_5	-4.23×10^{-3}	
ϵ_5	-1.033×10^{-3}	

[a] Reference 10.

It is worth pointing out that our extensions of the NWS model preserve the axially symmetric character of the dynamical model. Hence, the slab with free surfaces will satisfy the rotational invariance condition required for the lattice dynamics to agree with elastic theory in the limit of long waves.[12] This is in contrast to the case of a more general bulk Born–von Kârmân tensor force-constant model, which would not automatically satisfy such rotational invariance for the slab and which would probably require significant modification of force constants near the surface in order to recover rotational invariance.

The dynamical equations (7) are numerically solved for a mesh of wave vectors $\vec{q}$ in the irreducible part Γ*AHKLM* of the Brillouin zone (BZ) (see Fig. 2). For each $\vec{q}$ there are twelve ($p=1,2,\ldots,12$) modes, each with a frequency $\omega_p(\vec{q})$ and a twelve-component polarization vector $\vec{\xi}(\kappa;\vec{q}p)$.

C. Dispersion curves

In order to facilitate comparison of the bulk dispersion curves $\nu_p(\vec{q})$ [$=\omega_p(\vec{q})/2\pi$] with those of the slab, we present the bulk dispersion curves in the so-called *slab-adapted* form, i.e., the bulk dispersion curves are displayed as functions of the

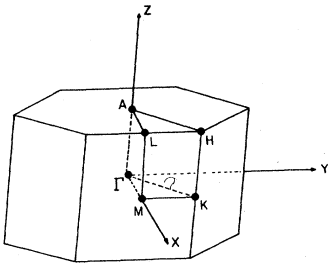

FIG. 2. Bulk graphite Brillouin zone.

two-dimensional (2D) wave vector $\bar{q}=(q_x,q_y)$ (two-dimensional vectors are indicated by a bar) instead of as functions of the three-dimensional (3D) vector $\vec{q}=(q_x,q_y,q_z)$. In such a graph one plots, for a given q_x,q_y interval, the family of dispersion curves with each member corresponding to one of the various allowed q_z values. The latter are determined by the number of layers that form the periodicity length in the z direction. For this we choose a number of layers closely approximating the number of layers in the slab. For details of this method we refer to Allen *et al.*[13]

In Fig. 3 we display the slab-adapted bulk dispersion curves for a z periodicity length of 14 planes, for $\bar{q}$ along the directions ΓM, MK, and $K\Gamma$ in the BZ (see Fig. 2). Since there are two atoms (six degrees of freedom) per plane and fourteen planes, this graph consists of 84 dispersion curves. They are clustered together in six bands of which the top three (bands 4,5,6) have virtual 14-fold degeneracy; in band 3 the virtual degeneracy is lifted only rather close to the origin Γ, while bands 1 and 2 are nondegenerate over larger portions of the BZ. This virtual degeneracy results from the very weak dependence of $\nu_p(\vec{q})$ on q_z, which is an expression of the large anisotropy of graphite resulting from the weakness of van der Waals interactions between the planes, as compared to the strong covalent interactions within the planes.

The dynamical characters of the slab-adapted bulk bands along Γ to M are of particular interest because the subsequent discussion of the bands of the slab with free surfaces focuses on this direction, for which the sagittal plane is a mirror plane. Along Γ to M there are three regions of "band crossing" away from the low-frequency complex near Γ, at $\bar{q}=0.6\bar{q}_M$, $0.8\bar{q}_M$, and $0.9\bar{q}_M$. We label the bulk bands $1,2,\ldots,6$ in strict increasing order of their frequency, except in the low-frequency complex near Γ. Thus, because of the apparent band crossings mentioned, the dynamical character of a band will change across such regions. We may describe the dynamical character of a mode by whether the polarization vector represents linear polarization perpendicular to the sagittal plane (SH, for shear horizontal) or elliptical polarization *in* the sagittal plane (SP); the latter classification can be further divided into SP polarization with the projection of the major axis largest in the direction of propagation ($\mathrm{SP}_{\parallel}$) or largest in the direction normal to propagation ($\mathrm{SP}_{\perp}$). For example, at $\bar{q}=0.5\bar{q}_M$, band 1 is $\mathrm{SP}_{\perp}$, 2 is SH, 3 is $\mathrm{SP}_{\parallel}$, 4 is $\mathrm{SP}_{\perp}$, 5 is SH, and 6 is $\mathrm{SP}_{\parallel}$. At $\bar{q}=\bar{q}_M$, after the three band crossings have been encountered, the dynamical character of bands 1 through 6 is, respectively, $\mathrm{SP}_{\perp}$, $\mathrm{SP}_{\perp}$, SH, SH, $\mathrm{SP}_{\parallel}$, and $\mathrm{SP}_{\parallel}$. In the SP classes, the highly anisotropic character of the interactions causes the polarization ellipses to be nearly degenerate linear polarizations; that is, the parallel components in an $\mathrm{SP}_{\perp}$ mode are always 3 or more orders of magnitude smaller than the normal components, and vice versa for $\mathrm{SP}_{\parallel}$. Thus, the apparent band crossing at $\bar{q}=0.6\bar{q}_M$ is avoided by hybridization of the $\mathrm{SP}_{\parallel}$ and $\mathrm{SP}_{\perp}$ character of bands 4 and 3, but because of the very weak interaction between x and z motions the two bands approach very near each other. On the other hand, at $\bar{q}=0.8\bar{q}_M$ and $0.9\bar{q}_M$, the apparent crossing along ΓM is real because there we have bands that are first SH and SP, and then SP and SH, touching in a cusp. When $\bar{q}$ leaves the ΓM mirror plane, this cusp rounds into the usual sort of hybridization gap because the pure symmetry character of SP and SH is lost; at general points in the slab-adapted Brillouin zone, there will be significant mixing of $\mathrm{SP}_{\parallel}$ and SH character because of the strong intraplanar couplings.

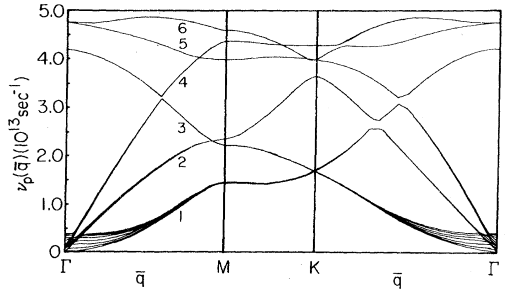

FIG. 3. Bulk graphite slab-adapted dispersion curves for $\bar{q}$ values along the directions ΓM, MK, and $K\Gamma$ of the Brillouin zone.

D. Frequency distribution

In order to evaluate the thermal properties of the crystal, one has to solve the dynamical equations for a sampling grid of $\vec{q}$ values throughout the irreducible part of the 3D BZ. The frequency distribution $g(\nu)$ has been obtained with the Gilat-Dolling-Raubenheimer method,[14,15] with which a smooth frequency distribution can be obtained from actual diagonalization of the dynamical equations for a quite limited set of $\vec{q}$ values.

In Fig. 4 we display the frequency distribution $g(\nu)$ for bulk graphite. The peaks in $g(\nu)$ (labeled A through I) correspond roughly with the flat portions of the dispersion curves in Fig. 3. By studying the vibrational character of the modes contributing to these flat portions, one can identify the kinds of modes that contribute to the various peaks in $g(\nu)$.

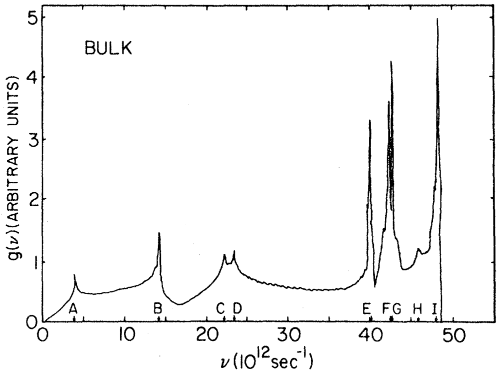

FIG. 4. Bulk graphite frequency distribution $g(\nu)$.

III. THE GRAPHITE SLAB

As was mentioned in the Introduction, the aim of this study is to lay the groundwork for a treatment of the dynamical and thermodynamic properties of gases adsorbed on graphite which takes full account of the dynamical coupling between adsorbate and adsorbent. The experimental results obtained in a companion study by one of us (*E.* de *R.*) pertain to adsorption studies on graphite samples with large surface-to-volume ratio.[16] To obtain the thermodynamic properties of the adsorbed gases *per se* (adsorbate), one has to subtract from the properties of the total adsorbate-adsorbent system those of the bare graphite (adsorbent). The dynamics of systems with large surface-to-volume ratio shows significant difference from the bulk dynamics through the occurrence of surface-localized vibrations and other changes in the frequency distribution, which consequently result in changes in the thermodynamic properties of such systems. The first step in this analysis is to study the dynamics of a thin graphite slab, which is the simplest system that exhibits a large surface-to-volume ratio, and for which the dynamics remains tractable.

A. Slab dynamics

As mentioned earlier, a graphite slab consists of a finite number of (0001) oriented graphite planes; the slab has two surfaces, and translational symmetry in the z direction ([0001] direction) does not exist. This has important consequences for the lattice-dynamical formulation. We briefly outline the main features of the "slab dynamics," following the work of Allen *et al.*[17] and referring to this work for details.

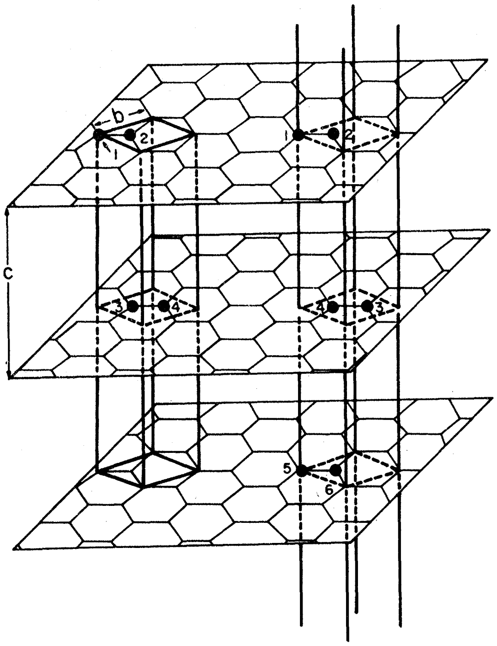

FIG. 5. Graphite slab unit cell. The unit cell extends through the entire thickness of the slab and contains two atoms for each layer in the slab.

Since, in the slab, periodicity exists only in the x and y directions, the slab unit cell extends through the entire thickness of the slab (see Fig. 5), and only 2D lattice vectors are needed to specify the position of a cell; of course, 3D vectors continue to be needed to specify the atomic position inside the cell. Furthermore, because of the 2D translational symmetry, the reciprocal lattice is 2D.

We introduce 2D vectors with only x and y components, and indicate these with superior bars: If $\vec{r}=(x,y,z)$ and $\vec{l}=(l_1,l_2,l_3)$, then $\bar{r}=(x,y)$ and $\bar{l}=(l_1,l_2)$. The position of the cell $\bar{l}$ is then $\bar{r}_0(\bar{l})=l_1\vec{a}_1+l_2\vec{a}_2$. The 2D reciprocal lattice is determined by the basis vectors

$$\bar{b}_1=2\pi\frac{\vec{a}_2\times\hat{z}}{\vec{a}_1\cdot\vec{a}_2\times\hat{z}}\,,\quad \bar{b}_2=2\pi\frac{\vec{a}_1\times\hat{z}}{\vec{a}_1\cdot\vec{a}_2\times\hat{z}}\,, \tag{14}$$

where $\hat{z}$ is the unit vector in the z direction. The corresponding 2D surface BZ (SBZ) is shown in Fig. 6. The symmetry points in the SBZ are labeled by barred letters (e.g., $\bar{\Gamma}$) to distinguish them from points in the 3D BZ (e.g., Γ).

As in the bulk case, the index κ will label the atoms in the unit cell. For a 13-layer slab, the unit cell contains $13\times2=26$ atoms; thus $\kappa=1,2,\ldots,26$ (note that in this notation the layer in

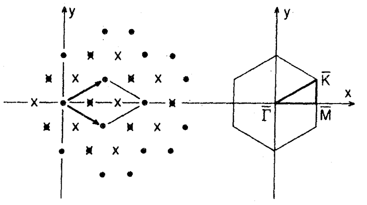

FIG. 6. Graphite planar-projected crystal structure and associated slab Brillouin zone.

which an atom resides is implicitly indicated in its κ value).

In analogy with Eq. (7) the slab eigenvalue equations are

$$\sum_{\kappa'\beta} D_{\alpha\beta}(\kappa\kappa';\bar{q})\xi_\beta(\kappa';\bar{q}p) = \omega_p^2(\bar{q})\xi_\alpha(\kappa;\bar{q}), \qquad (15)$$

where the dynamical matrix elements are given by

$$D_{\alpha\beta}(\kappa\kappa';\bar{q}) = (M_\kappa M_{\kappa'})^{-1/2} \sum_{\bar{l}} \Phi_{\alpha\beta}(\bar{l}\kappa;\bar{l}'\kappa') \exp\{i\bar{q}\cdot[\bar{r}_0(\bar{l}') - \bar{r}_0(\bar{l}) + \bar{r}_0(\kappa') - \bar{r}_0(\kappa)]\}. \qquad (16)$$

The construction of the dynamical matrix is done in the same way as for the bulk, the only differences being that the number of atoms in the unit cell is larger and that the "self-interaction" matrix elements are modified because of missing neighbors. For a slab consisting of thirteen layers, having two carbon atoms per layer in the slab unit cell, the order of the dynamical matrix is 13 × 2 × 3 = 78. With respect to the reduction of the dynamical matrix, the same symmetry operations apply as for the bulk, except for the lack of translations in the z direction. The construction of the elements of the dynamical matrix is done by rotational transformations on a minimum set of 3 × 3 matrices, in a manner similar to the bulk case. For details we refer to Ref. 18.

B. Surface modes

In surface vibrational modes the surface atoms have large vibrational amplitudes, while atoms deeper inside the crystal have vanishingly small amplitudes. These vibrations may be identified by an examination of the polarization vectors $\vec{\xi}(\kappa;\bar{q}p)$ for fixed wave vector $\bar{q}$ and given polarization p. It is convenient to decompose the index κ into two indices (m,i), where m labels the atomic plane and i labels the two different atoms in each plane. Then, for fixed $\bar{q}$ and p we examine the quantity

$$|\vec{\xi}(m)|^2 = |\xi_x(m)|^2 + |\xi_y(m)|^2 + |\xi_z(m)|^2, \qquad (17)$$

where, for example, $m = 1$, 13 labels the top and bottom planes, respectively, of a 13-layer slab. In Eq. (17) we have suppressed the index i because it turns out that the square amplitudes for the two different atoms in each plane differ by less than 1% in all cases examined. For a surface mode $|\vec{\xi}(m)|^2$ decreases rapidly with increasing m down to the middle of the slab, and then increases rapidly again as the bottom surface is approached. For a systematic description of the kinds of surface modes that can occur in general, we refer to Allen *et al.*[13] In contrast to the surface modes, $|\vec{\xi}(m)|^2$ for a bulk mode exhibits no surface localization.

In Fig. 7 we show the slab dispersion curves of a 13-layer slab for wave vectors $\bar{q}$ chosen along the ΓM direction in the SBZ (cf. Fig. 6). Notice that these curves look very much like the slab-adapted bulk dispersion curves along ΓM in Fig. 3. As was the case with the latter, the 78-slab dispersion curves fall into six bands and also exhibit a high order of near degeneracy (approximate degeneracy in each band over most of Fig. 7).

There is, however, a significant difference with the bulk case which is not visually evident in Fig. 7: An examination of the functions $|\vec{\xi}(m)|^2$ vs m for each of the 78 modes shows that each band contains two degenerate modes, with frequencies slightly below those of the other eleven bulk modes in the band, for which $|\vec{\xi}(m)|^2$ decreases rapidly

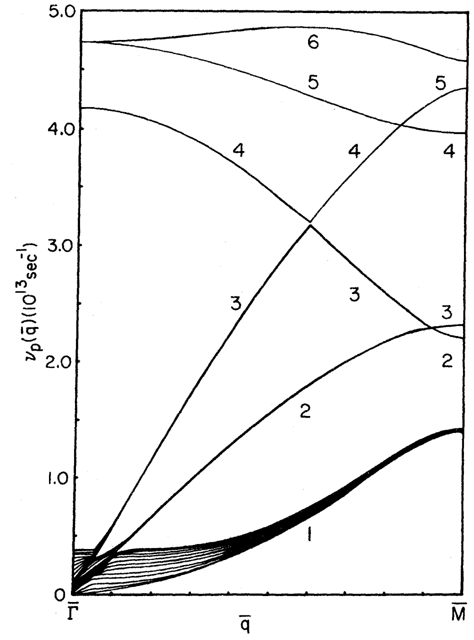

FIG. 7. Graphite slab dispersion curves for $\bar{q}$ values along the direction $\bar{\Gamma}\bar{M}$ in the SBZ.

going into the slab; these are *surface modes*. It is a common occurrence for surface modes to be "peeled off" from the bottom of bulk bands (cf. Allen *et al.*[13]). We label these pairs of surface modes in bands 1 through 6, S_1 through S_6, respectively. They have polarizations of SP$_{\parallel}$, SH, and SP$_{\perp}$ character in common with those of their respective bulk bands.

The three lowest surface modes in bands 1, 2, and 3, which include the familiar Rayleigh mode, are *macroscopic*[19(a)] and *quasimacroscopic*[19(b)] surface modes; this means that their amplitude dimenishes exponentially away from the surface, with decay lengths that scale according to some low power of the wavelength for long wavelengths. For these modes, $\nu_p(\bar{q}) \rightarrow 0$ as $\bar{q} \rightarrow 0$, corresponding to the three rigid-body translations of the crystal. The three higher surface modes in bands 4, 5, and 6 are, on the other hand, microscopic surface modes in the sense that at long wavelengths their decay lengths scale according to the lattice constants.

In Figs. 8–10 we display attenuation curves for the square amplitudes $|\vec{\xi}(m)|^2$ of surface modes S_1 through S_6 for wave vectors along $\overline{\Gamma M}$. The principal polarization character of the modes is, as in the previous discussion of the bulk bands,

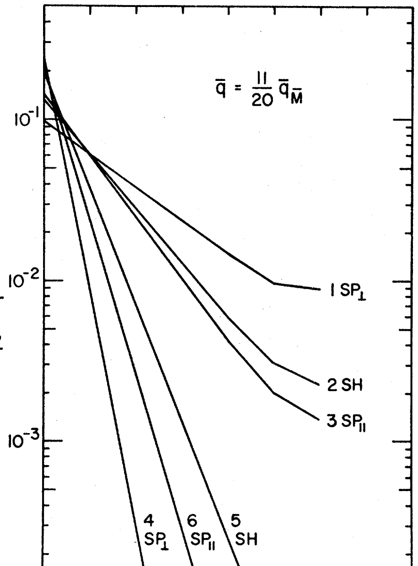

FIG. 8. Attenuation with depth of the surface vibrational modes of graphite at $\bar{q}=\frac{11}{20}\bar{q}_{\bar{M}}$. The numeral indicates the bulk band with which the surface mode is most associated, and the dynamical character of the surface modes is denoted SH, SP$_\parallel$, or SP$_\perp$ as appropriate. The value of $|\vec{\xi}(m)|^2$ plotted is the arithmetic average of the even and odd members of the slab surface mode pair for one atom in each layer. $|\vec{\xi}(m)|^2$ is normalized so that the sum over all layers and both atoms in each layer yields unity. [Note: $|\vec{\xi}(m)|^2$ differs between the two atoms in each layer by less than one percent, except near the middle of the slab.]

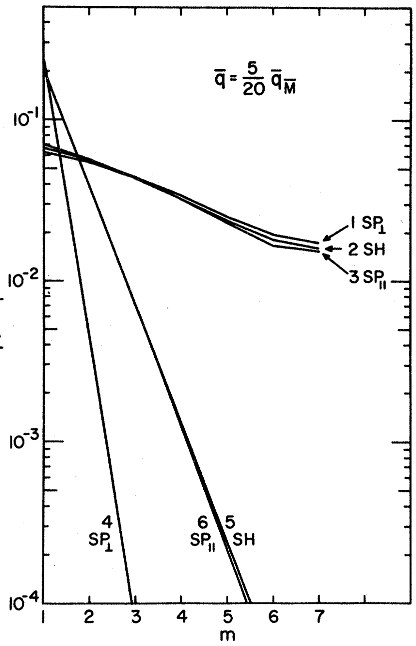

FIG. 9. Attenuation with depth of the surface vibrational modes of graphite at the SBZ boundary $\bar{q}=\frac{5}{20}\bar{q}_{\bar{M}}$. Conventions followed are given in the caption of Fig. 8.

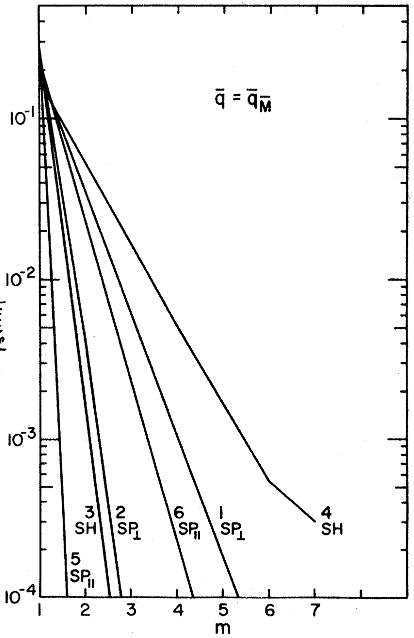

FIG. 10. Attenuation with depth of the surface vibrational modes of graphite at $\bar{q}=\bar{q}_{\bar{M}}$. Conventions are given in the caption of Fig. 8. (Note that the dynamical character indications for branches 2, 3, 4, and 5 have changed from Figs. 8 and 9 because of hybridization.)

$\mathrm{SP}_\perp$ (elliptical polarization in the sagittal plane with more vertical than horizontal component), $\mathrm{SP}_\parallel$ (elliptical polarization in the sagittal plane with more horizontal than vertical component), and SH (shear horizontal; linear polarization with particle motion perpendicular to the sagittal plane). Although the separation into elliptical polarization (in the sagittal plane) and linear polarization (normal to the sagittal plane) is rigorously true only along $\overline{\Gamma M}$ [for which the sagittal plane is a plane of mirror symmetry (see Fig. 6)], polarization characters persist in a qualitative sense even along $\overline{\Gamma K}$, where the sagittal plane lies midway between two adjacent vertical mirror planes. Note, however, that, as with the slab-adapted bulk bands, we have numbered the surface bands in a strictly increasing order of increasing frequency at each wave vector of the SBZ. Essentially the same considerations of symmetry decoupling between SP and SH modes and its effects on hybridization gaps, which were applied in the discussion of the slab-adapted bulk dispersion curves, apply equally to the case of dispersion curves of the slab with free surfaces. Hence, near the SBZ, boundary surface bands 2, 3, 4, and 5 (and of course their parent bulk bands) have polarization characters different from those they had in the first half of the SBZ.

Figure 8 corresponds to a wave vector along $\overline{\Gamma M}$ about halfway to the SBZ boundary, $\bar{q}=\frac{11}{20}\bar{q}_{\bar{M}}$. The near-linear behavior of these semilogarithmic curves from the surface layer ($m=1$) through the four or so subsurface layers indicates that at this wave vector the variation with depth of each surface mode is dominated by a single decaying exponential which is characteristic of the individual surface mode. While we have not solved for the evanescent waves of the bulk phonon band structure, the appearance of this dominant behavior of the surface-mode amplitude indicates that each surface mode is made up predominantly of a single evanescent wave having the imaginary component of wave vector normal to the basal planes, $\alpha = \mathrm{Im}(q_z)$; that is, the vibrational amplitude is closely approximated as

$$\xi(m) \propto \exp(-\alpha m c)\,, \tag{18}$$

where c is the fundamental interplanar distance. [Lack of structure within this envelope indicates that for this dominant evanescent wave $\mathrm{Re}(q_z) \ll (6c)^{-1}$.] Hence α can be read off from straight-line portions of the attenuation curves, so that in Fig. 8 at $\bar{q}=\frac{11}{20}\bar{q}_{\bar{M}}=2\pi/\lambda$ the principal decay length (α^{-1}) ranges from about $4\frac{1}{4}$ interplanar distances for S_1 (the macroscopic Rayleigh mode) down to 0.6 interplanar distances for S_4.

Figures 9 and 10 give attenuation curves at two other representative wave vectors along $\overline{\Gamma M}$: $\bar{q}=\frac{5}{20}\bar{q}_{\bar{M}}$, for which the wavelength is fairly long, yet for which the higher-lying bands are well clear of the broad bulk band 1, and $\bar{q}=\bar{q}_{\bar{M}}$, at the SBZ boundary. We note that at all these wave vectors, the surface-mode amplitudes appear to be dominated by a single evanescent wave. The wave vector of the dominant evanescent wave must be purely imaginary, because the attenuation curves do not exhibit any oscillatory behavior. [The breaks in slope shown between the $m=6$ layer and the middle layer of the slab ($m=7$) are artifacts of the limited thickness of the slab. The surface modes occur in nearly degenerate pairs, with the odd member of a pair having a node at the midplane for any (x, y) components of displacement and the even member of the pair having a node there in any z components. Thus, for the more deeply penetrating modes there is an appreciable nonvanishing amplitude at the midplane which is manifest as a break in the slopes in Figs. 8–10; the break in slope can be observed to become less significant as the modes become less deeply penetrating with decreasing wavelength.]

The ratio α^{-1}/λ for the Rayleigh mode changes only about 7% as $\bar{q}$ ranges from $\frac{11}{20}\bar{q}_{\bar{M}}$ to $\frac{5}{20}\bar{q}_{\bar{M}}$ (at this shorter wave vector, the Rayleigh mode exhibits only a semiquantitatively exponential behavior in Fig. 9), whereas this ratio varies much more widely for the other five surface modes over the same wave-vector change. The proportionality of α^{-1} to wavelength is a characteristic of Rayleigh waves derived for elastic continua, and we see that this feature still obtains approximately for wave vectors at least halfway to the SBZ boundary. Of course, as the wave vector more closely approaches the SBZ boundary where the wavelength satisfies the Bragg condition, the effect of microscopic periodicity of the lattice can be expected to modify the "macroscopic" characteristics of S_1; e.g., for $\bar{q}=\bar{q}_{\bar{M}}$ (Fig. 10), α^{-1}/λ for S_1 is 1.20, only some 70% of the roughly constant value of 1.75 it had over the first half of the distance to the SBZ boundary. While we do not know of any calculations of α^{-1} for the Rayleigh mode based on elastic continuum theory which can be compared with our results, Dobrzynski and Maradudin[20] have obtained a general formula for the Rayleigh wave velocity v_R on a basal surface of an elastic medium of hexagonal symmetry, and as applied to graphite this result reinforces our finding of a very slight splitting of surface mode branches from their parent bulk bands. The relation for the Rayleigh wave velocity can be put into the form

$$\begin{aligned}(\chi_R^2-1)[\chi_R^2-c_{11}/c_{44}+c_{13}^2/(c_{33}c_{44})]^2\\ =(c_{44}/c_{33})\chi_R^4(\chi_R^2-c_{11}/c_{44})\,,\end{aligned} \tag{19}$$

where $\chi_R = v_R/(c_{44}/\rho)^{1/2}$ is the Rayleigh wave velocity scaled by the velocity driven by the c_{44} elastic constant. For single-crystal graphite, nominal values for the elastic constants are[21] (in units of 10^{10} N m^{-2}) $c_{11}=106$, $c_{66}=44$, $c_{33}=3.65$, $c_{13}=1.50$, and $c_{44}=0.40$. With these values it is readily apparent that χ_R will be only slightly less than unity, and in fact Eq. (19) yields a solution of $\chi_R^2=0.9996$, accurate to 2 parts in 10^5 if χ_R^2 is set to unity everywhere except in the (χ_R^2-1) factor. Hence, in the long-wavelength limit the Rayleigh wave frequency is split down only 0.02% from the bulk mode governed by c_{44}.

Although we do not show dispersion or mode attenuation curves for wave vectors along $\overline{\Gamma K}$ or in the interior of the irreducible element of the SBZ, it should be obvious from an examination of the bulk bands of Fig. 3 and our discussion of Figs. 7–10 that many features will parallel those we have discussed already. The primary differences are those following from the lack of a vertical mirror plane symmetry. Although the hybridization regions shown in the ΓK panel of Fig. 3 are slightly exaggerated by being plotted as straight line segments connecting a 20-point mesh, they are still substantial because of the lower symmetry.

C. Slab frequency distribution

The slab frequency distribution $g^{\rm slab}(\nu)$ is of importance for the calculation of the thermodynamic properties of the slab (to be discussed in a subsequent paper). Of particular interest are any features in $g^{\rm slab}(\nu)$ that result from the surface modes; to reveal these we have to compare $g^{\rm slab}(\nu)$ with the bulk frequency distribution $g^{\rm bulk}(\nu)$.

The main difficulty in evaluating an accurate slab frequency distribution is the fact that the Gilat *et al.*[14,15] method has not yet been adapted for surface calculations.[22] In the present work we therefore employed the straightforward root-sampling method [cf. Eq. (14)]. In order to enhance the accuracy of $g^{\rm slab}(\nu)$ at low frequencies (which is important for low-temperature thermodynamic properties) we divided the irreducible element of the SBZ into three regions: an outer region covering $\frac{8}{9}$ths of the zone and containing 264 uniformly distributed sampling points, an intermediate region covering $\frac{8}{81}$ths of the zone, also containing 264 sampling points, and an inner region, covering $\frac{1}{81}$ths of the zone and containing 300 sampling points.

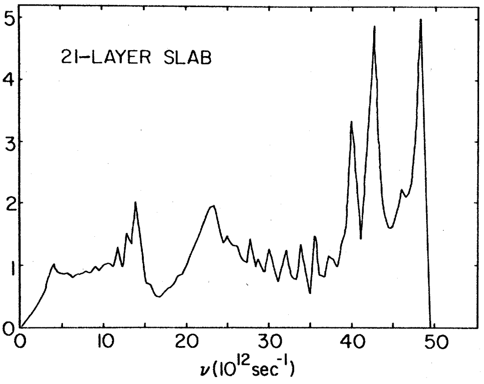

FIG. 11. Slab frequency distribution $g^{\rm slab}(\nu)$ for a 21-layer graphite slab. The number of frequency channels used is 100.

In Fig. 11 we show $g^{\rm slab}(\nu)$ for a 21-layer slab; it was constructed by using 100 frequency intervals between 0 and 5.5×10^{13} Hz. In comparison with the bulk $g^{\rm bulk}(\nu)$ (Fig. 4), which was generated with the Gilat *et al.* method, it is clear that a fair amount of "noise" is present in $g^{\rm slab}(\nu)$; this is a result of the much smaller number of frequencies available in the straight sampling method. Nevertheless, the main features, i.e., the peaks, which we observed in $g^{\rm bulk}(\nu)$, are also present in $g^{\rm slab}(\nu)$, but at slightly lower frequencies; however, the peaks C, D, F, and G in $g^{\rm bulk}(\nu)$ are not resolved in $g^{\rm slab}(\nu)$. Those peaks which result from noise only (especially between 25 and 38×10^{12} Hz) were identified by comparing their positions for 3- and 13-layer slabs (not shown here) and for the 21-layer slab; the positions of the noise peaks shift when changing the slab thickness, whereas the positions of the physically significant peaks do not shift. The great similarity between $g^{\rm slab}(\nu)$ and $g^{\rm bulk}(\nu)$ (aside from the noise features) is a direct result of the great weakness of the interplanar forces relative to the intraplanar forces: The creation of the surfaces causes only a relatively small perturbation of the bulk dynamics, in contrast to the situation in more isotropic crystals (cf. Ref. 13). Nevertheless, it is precisely the subtle differences between $g^{\rm slab}$ and $g^{\rm bulk}$ which give rise to surface-excess thermodynamic properties. Similar subtle differences between slab and bulk for the layer- (and polarization-) projected frequency distributions, formed by weighting mode contributions to $g(\nu)$ with the appropriate components of the mode eigenvectors, give rise to surface-excess dynamical quantities such as surface enhancements of the mean-square amplitudes of vibration. A more detailed discussion of these questions requires more work and must be left to subsequent papers; a preliminary discussion of the question of surface-excess specific heat was given in Ref. 9.

IV. CONCLUSIONS

We have shown that an extension of the NWS axially symmetric model for graphite lattice dynamics leads to the existence of surface-localized vibrational modes associated with every bulk band and existing over all of the surface Brillouin zone. Through the inner half of the SBZ, the three lowest surface-mode branches exhibit macroscopic and quasimacroscopic character: S_1 is the Rayleigh wave branch, which is entirely macroscopic and is directionally isotropic at long wavelength; S_2 and S_3 are quasimacroscopic (in that their localization scales as a low power of wavelength), at least as soon as their parent bulk bands have cleared the low-lying broad bulk band extending up to about 4 THz. In this low-lying bulk band S_2 and S_3 are only pseudo-surface-waves (i.e., resonances), except that exactly along the $\overline{\Gamma M}$ direction S_2 remains a quasimacroscopic surface wave, decoupled by symmetry from the surrounding bulk band. The higher-lying surface bands S_4, S_5, and S_6 are microscopic (in that their localization scale is determined by lattice constants) over the entire SBZ.

Unlike the wide variety of structures in the surface mode shapes found in earlier work on cubic and hcp crystals (e.g., Refs. 13, 23–25), the mode shapes [described by $|\vec{\xi}(m;\bar{q})|^2$] for each of the surface mode branches exhibit a simple layer-to-layer exponential decay over the whole SBZ, including the SBZ boundary. This means that each surface branch is dominated by a single evanescent wave (of the complex bulk band structure[26]) characteristic of that branch, and, furthermore, the complex wave vector q_z of the dominant mode is pure imaginary (any real part of q_z would give an oscillatory modulation to the exponential decay given by the imaginary part).

In another contrast with results obtained with crystals of only moderate anisotropy, the surface bands of graphite (0001) are peeled down from their respective bulk bands by only very, very slight frequency shifts. Even the Rayleigh branch differs in sound velocity from the bottom edge of its parent bulk band by only a small fraction of 1%. This has the consequence that the surface-excess frequency distribution $g^s(\nu)$ $[\propto g^{\text{slab}}(\nu) - g^{\text{bulk}}(\nu)]$ deviates from its mean value of zero by positive and negative excursions that are much smaller than those found for surfaces of crystals with more moderate anisotropy, because for all except the lowest bulk band the narrowness of the bulk bands in comparison to their dispersion across the SBZ means that any positive contribution to $g^s(\nu)$ from a surface mode at any point in the SBZ is largely canceled by the associated depletions of its parent bulk band at nearby points of the SBZ. This self-cancellation of $g^s(\nu)$ holds less strongly for the contributions from S_1 and its parent bulk band; however, it is still much stronger in graphite (0001) than more moderately anisotropic crystals, and the smallness of variation in $g^s(\nu)$ for graphite (0001) supports the usual practice in adsorption studies using this substrate of neglecting the contribution of the surface dynamics of graphite (one aspect of the "inert-adsorbent" approximation). A preliminary report of the effect of the residual $g^s(\nu)$ for graphite (0001) on the surface-excess specific heat has been given in Ref. 9, and more detailed reports of the temperature-dependent properties such as surface thermodynamic functions and surface-enhanced mean-square amplitudes are in preparation.

ACKNOWLEDGMENTS

We thank Dr. R. M. Nicklow for helpful comments on the lattice dynamics of bulk graphite and for supplying us with a copy of a Gilat-Raubenheimer-type computer program for calculating the frequency distribution of bulk graphite. One of us (F. W. de W.) acknowledges research support by the National Science Foundation under Grant No. DMR 7810309 and the Robert A. Welch Foundation.

---

[1] W. de Sorbo and G. E. Nichols, J. Phys. Chem. Solids 6, 352 (1958).

[2] J. C. van der Hoeven and P. M. Keesom, Phys. Rev. 130, 1318 (1963).

[3] P. Delhaes and Yoshihiro Hishiyama, Carbon 8, 31 (1970).

[4] G. H. Wostenholm and B. Yates, Philos. Mag. 27, 185 (1973).

[5] K. Komatsu, J. Phys. Chem. Solids 8, 380 (1958).

[6] P. Flubacher, A. J. Leadbetter, and J. A. Morrison, J. Phys. Chem. Solids 13, 160 (1960).

[7] (a) G. Albinet, J. P. Biberian, and M. Bienfait, Phys. Rev. B 3, 2015 (1971); (b) J. P. Biberian, M. Bienfait, and J. B. Theeten, Acta Crystallogr. A 29, 221 (1973). These works use a simple first-neighbors model (with five force constants related to the elastic constants) to discuss primarily the mean-square amplitudes of bulk and surface vibrations of graphite. This model underestimates by some 20% the low-lying LO branch along the [0001] direction which corresponds to opposing motion of adjacent (0001) planes [see Ref. 7(b)].

[8] (a) J. Suzanne, P. Masri, and M. Bienfait, Surf. Sci. 43, 441 (1974); Jpn. J. Appl. Phys. 1974, Suppl. 2, part 2, pp. 295–298; (b) J. P. Coulomb, J. Suzanne, M. Bienfait, and P. Masri, Solid State Commun. 15, 1585 (1974); (c) J. P. Coulomb and P. Masri, *ibid.* 15, 1623 (1974). These works examine various aspects (especially surface entropy and mean-square vibrational amplitudes) of Xe and Kr adsorbed on graphite, using a simple force-constant model

restricted to nearest-neighbor interactions. Papers (a) and (b) keep the graphite substrate static, while (c) examines a dynamically coupled two-plane model—a single dynamic plane of graphite bearing an adsorbed monolayer.

[9] E. de Rouffignac, G. P. Alldredge, and F. W. de Wette, Chem. Phys. Lett. 69, 29 (1980).

[10] R. Nicklow, N. Wakabayashi, and H. G. Smith, Phys. Rev. B 5, 4951 (1972).

[11] *American Institute of Physics Handbook*, 3rd ed., edited by D. E. Gray (McGraw-Hill, New York, 1972), p. 905.

[12] A. A. Maradudin, E. W. Montroll, G. H. Weiss, and I. P. Ipatova, *Theory of Lattice Dynamics in the Harmonic Approximation*, 2nd ed. (Academic Press, New York, 1971), Chap 1.

[13] R. E. Allen, G. P. Alldredge, and F. W. de Wette, Phys. Rev. B 4, 1661 (1971).

[14] G. Gilat and G. Dolling, Phys. Lett. 8, 304 (1964).

[15] G. Gilat and L. J. Raubenheimer, Phys. Rev. 144, 320 (1966); L. J. Raubenheimer and G. Gilat, Phys. Rev. 157, 586 (1967).

[16] E. de Rouffignac and W. H. Wade, J. Chem. Phys. 74, 3598 (1981).

[17] R. E. Allen, G. P. Alldredge, and F. W. de Wette, Phys. Rev. B 4, 1648 (1971).

[18] E. P. de Rouffignac, Ph. D. thesis, University of Texas at Austin, 1979 (unpublished). Available as Order No. 79-20103 from University Microfilms International, P. O. Box 1764, Ann Arbor, Michigan 48106.

[19] (a) The Rayleigh wave of elastic continuum theory is a truly macroscopic surface wave in that it exists (*when* it exists) at the long-wavelength limit at a velocity lower than the associated bulk velocity, and its localization depth scales as the wavelength of propagation. See, for example, the review by G. W. Farnell, in *Physical Acoustics*, edited by W. P. Mason and R. N. Thurston (Academic, New York, 1970), Vol. 6, pp. 106–166. (b) On the other hand, what we here call quasimacroscopic surface waves do not exist as identifiable macroscopic surface excitations at the *limit* of long wavelengths, but they are so identifiable in the *regime* of long wavelengths (i. e., at finite but arbitrarily long wavelengths). At long wavelengths, their frequency separation from the associated bulk bands scales as λ^{-s} ($s > 0$) and their localization depth scales as λ^{l} ($l > 1$), where λ is the propagation wavelength. Although these modes appeared in the earliest crystal slab calculations of R. E. Allen, G. P. Alldredge, and F. W. de Wette (see, e.g., Ref. 13 above), their quasimacroscopic character was first elucidated by G. P. Alldredge, Phys. Lett. A 41, 281 (1972) [for the (001) surface of a simple cubic crystal]. Subsequent work has explored the domain of existence of such waves for other surfaces; for example, for the (001) surface of bcc crystals, see V. L. Zoth, G. P. Alldredge, and F. W. de Wette, Phys. Lett. A 47, 247 (1974).

[20] L. Dobrzynski and A. A. Maradudin, Phys. Rev. B 14, 2200 (1976); 15, 2432 (E) (1977).

[21] O. L. Blakslee, D. G. Proctor, E. J. Seldin, G. B. Spence, and T. Weng, J. Appl. Phys. 41, 3373 (1970); E. J. Seldin and C. W. Nezbeda, *ibid.* 41, 3389 (1970).

[22] Our attempts to adapt the Gilat-Dolling-Raubenheimer method to the slab case has so far had only partial success. The $g^{\mathrm{slab}}(\nu)$ curves obtained so far still contain spurious kinks and maxima which makes the $g^{s}(\nu)$ so obtained unsuitable for the calculation of the thermal functions. It is believed that these difficulties in $g^{\mathrm{slab}}(\nu)$ arise from band crossings and degeneracies occuring at small wave vectors (cf. Fig. 7).

[23] R. E. Allen, G. P. Alldredge, and F. W. de Wette, Phys. Rev. B 6, 632 (1972): hcp (0001) surface.

[24] T. S. Chen, G. P. Alldredge, F. W. de Wette, and R. E. Allen, Phys. Rev. B 6, 627 (1972); T. S. Chen, F. W. de Wette, and G. P. Alldredge, *ibid.* 15, 1167 (1977): (001) face of various crystals having rocksalt structure.

[25] V. L. Zoth, G. P. Alldredge, and F. W. de Wette, Bull. Am. Phys. Soc. 20, 489 (1975) and unpublished results; V. L. Zoth, M. A. thesis, University of Texas at Austin, 1974 (unpublished) (available as technical report AFOSR-TR-74-1256 from National Technical Information Service, Springfield, VA 22151; specify NTIS Accession No. AD-783 259/5GA): bcc (001) and (110) surfaces.

[26] See, for example, F. W. de Wette and G. P. Alldredge, in *Methods of Computational Physics*, edited by G. Gilat, B. Adler, S. Fernbach, and M. Rotenberg (Academic, New York, 1976), Vol. XV, pp. 153–213, especially Sec. II C and references cited therein.